

Pulsar magnetic alignment and the pulsewidth-age relation

M. D. T. Young^{1*}, L. S. Chan², R. R. Burman² and D. G. Blair²

¹International Centre for Radio Astronomy Research, M468, University of Western Australia, 7 Fairway, Crawley, WA 6009, Australia

²School of Physics, M013, University of Western Australia, 35 Stirling Hwy, Crawley, WA 6009, Australia

Accepted 2009 October 30. Received 2009 October 30; in original form 2009 October 07

ABSTRACT

Using pulsewidth data for 872 isolated radio pulsars we test the hypothesis that pulsars evolve through a progressive narrowing of the emission cone combined with progressive alignment of the spin and magnetic axes. The new data provide strong evidence for the alignment over a time-scale of about 1 Myr with a log standard deviation of around 0.8 across the observed population. This time-scale is shorter than the time-scale of about 10 Myr found by previous authors, but the log standard deviation is larger. The results are inconsistent with models based on magnetic field decay alone or monotonic counter-alignment to orthogonal rotation. The best fits are obtained for a braking index parameter, $n_\gamma \approx 2.3$, consistent the mean of the six measured values, but based on a much larger sample of young pulsars. The least-squares fitted models are used to predict the mean inclination angle between the spin and magnetic axes as a function of log characteristic age. Comparing these predictions to existing estimates it is found that the model in which pulsars are born with a random angle of inclination gives the best fit to the data. Plots of the mean beaming fraction as a function of characteristic age are presented using the best-fitting model parameters.

Key words: pulsars: general – stars: evolution – stars: magnetic fields – stars: neutron.

1 INTRODUCTION

One of the greatest of the many mysteries of radio pulsars is their evolutionary histories. As pulsars age, powerful electromagnetic torques act to increase the rotation period, P , of the strongly magnetized neutron star, causing the spin-frequency, $\nu = 1/P$, to decrease over time, a phenomenon known as spin-down. This can be described by the equation

$$\dot{\nu} = -K\nu^n, \quad (1)$$

where n is a parameter known as the braking index, with $n = 3$ for a magnetic dipole rotating in a vacuum. The spin-down torque acting on the star is proportional to $\dot{\nu}$, and it decays over time as $\dot{\nu}$ decreases.

There is also evidence that K is not constant, but rather is also changing over time. The surface dipole magnetic field strength at the magnetic equator, assuming that the spin and magnetic axes are orthogonal, is conventionally given by $B_{\text{surf}} = 3.2 \times 10^{19} (P\dot{P})^{1/2}$ G; at the magnetic poles the field strength is $2B_{\text{surf}}$ (Lyne & Smith 2006). B_{surf} tends to be bigger for younger pulsars than for older ones having a large spin-down age, $t_s \equiv P/[(n-1)\dot{P}]$. This in turn suggests that K tends to reduce with increasing age, and much conjecture remains about the origin(s) of this evolution.

Many authors have argued that the main contributor to the K -evolution is the progressive alignment of the spin and

magnetic axes: e.g. Candy & Blair (1983), Candy & Blair (1986), Lyne & Manchester (1988), Xu & Wu (1991), Kuz'min & Wu (1992), Candy (1993), Pandey & Prasad (1996), Tauris & Manchester (1998) and Weltevrede & Johnston (2008). But McKinnon (1993) and Gil & Han (1996) have argued in favour of a random distribution of the inclination angles between the angular velocity and magnetic axes and against magnetic alignment. Others have favoured magnetic field decay (e.g. Narayan & Ostriker 1990), while there are also authors who argue for continuing counter-alignment to eventual orthogonality of the axes, via an electromagnetic torque exerted by magnetospheric electric currents flowing on open field lines (Beskin et al. 1984).

According to Jones (1976), pulsars initially counter-align (via a strongly temperature-dependent dissipative torque in the fluid interior) to reach the orthogonal rotator state after about 10^3 yr, where they remain for 10^4 – 10^5 yr (while the dissipative torque decays as the interior cools), after which alignment (via electromagnetic torque) occurs.

If K were constant, the braking index n would be equal to the apparent braking index,

$$n_{\text{app}} \equiv \nu\ddot{\nu}/\dot{\nu}^2 = 2 - P\ddot{P}/\dot{P}^2. \quad (2)$$

If $\ddot{\nu}$ can be determined from observations of a pulsar, then n_{app} can be computed. However, if K is varying, then in general $n_{\text{app}} \neq n$. Some authors (eg. Johnston & Galloway 1999; Tauris & Konar 2001) have argued that, for pulsars of moderate age, n_{app} exceeds the value of 3 that corresponds to magnetic dipole radiation. This could be taken to imply that either magnetic alignment or field de-

* E-mail: Matthew.Young@icrar.org

cay must be occurring. However, it is likely that recovery from unseen pulsar glitches is the principal contribution to measured variations in \dot{P} (Wang et al. 2001) for these pulsars.

In this paper, we shall use the pulsar evolution models from Candy & Blair (1983, hereafter CB83), Candy & Blair (1986, hereafter CB86) and Candy (1993, hereafter C93), which all invoke a progressive alignment of the spin and magnetic axes. The CB83 model develops the pulsewidth-age relation on the assumption that all pulsars move along the same evolutionary track, differing only in age and orientation with respect to Earth. The CB86 model relaxes this assumption and allows a distribution of alignment time-scales, as well as a time-varying relationship between characteristic and actual age. The C93 models additionally allow a distribution of initial inclination angles. All of these models predicted a minimum in the mean pulsewidth as a function of characteristic age and provided a good fit to the available data, consisting of 293 pulsewidth values from the Manchester & Taylor (1981) catalogue.

Here we use the ATNF (Australia Telescope National Facility) pulsar catalogue¹ (Manchester et al. 2005), version 1.35, to investigate pulsar evolution through magnetic alignment using the Candy–Blair models. This contemporary catalogue contains much larger data sets of 872 and 1420 isolated radio pulsars with 10 per cent and 50 per cent intensity pulsewidth values, W_{10} and W_{50} . It also contains many more old pulsars than was previously the case, which tend to have lower radio luminosities. It thus allows a more precise analysis of pulsar evolution. As a consistency check, we also examine separately those pulsars with pulsewidths measured during the Parkes multibeam pulsar survey (Manchester et al. 2001; Lorimer et al. 2006), giving W_{10} and W_{50} data sets of 377 and 934 pulsars respectively.

The paper is structured as follows. Section 2 presents a summary of the theory of alignment between the spin and magnetic axes; Section 3 gives a mathematical description of pulsewidth evolution; in Section 4 we least-squares fit the evolutionary pulsewidth models to the W_{10} and W_{50} data as functions of characteristic age; in Section 5 we further analyse these results, in particular comparing them to the inclination angle estimates of Rankin (1993b) and Gould (1994); and conclusions are presented in Section 6.

2 MAGNETIC ALIGNMENT THEORY

2.1 Evolution in true age

The Candy–Blair pulsar evolution models are based on two effects. One is progressive alignment of the spin and magnetic axes, for which the formula describing the alignment phase of the Jones (1976) model is adopted: this has an exponential decay of the sine of the magnetic-spin inclination angle, α , from its initial value α_0 :

$$\sin \alpha(t) = \exp(-t/\tau) \sin \alpha_0, \quad (3)$$

where t is the pulsar’s age and τ is the alignment time-scale. The alignment has a simple electromechanical origin: the electromagnetic radiation emitted by an oblique rotating dipole results in a torque on the star that causes the angular velocity axis to migrate through the neutron star toward alignment with the magnetic axis.

The second effect is progressive narrowing of the emission cone, described by a power-law dependence of its half-angle, ρ , on the rotation period, P :

$$\rho(t) \propto P^{-\gamma}(t), \quad (4)$$

with γ a positive constant having a value between 1/3 and 2/3 (Gunn & Ostriker 1970; Ruderman & Sutherland 1975; Lyne & Manchester 1988; Rankin 1993a).

For a pulsar with constant rotational inertia and fixed magnetic moment vector, the rotation period evolves according to $\dot{P}P^{n-2} = \text{constant}$. It was pointed out long ago (Phinney & Blandford 1981) that this simple rule is incompatible with the observed distribution of pulsars in the P – \dot{P} plane, conflicting with stationary ‘flow’ through that plane to pulsar ‘death’ at advanced ages. However, alignment produces an effective reduction in the magnetic moment, reducing the torque in proportion to $\sin^2 \alpha$; so, in the Jones model, the period evolves according to (Phinney & Blandford 1981)

$$\dot{P}P^{n-2} \propto \exp(-2t/\tau), \quad (5)$$

with n (the braking index) constant.

Equation (5) integrates to give:

$$P^{n-1}(t) = P_\infty^{n-1} + (P_0^{n-1} - P_\infty^{n-1}) \exp(-2t/\tau), \quad (6)$$

where P_0 is the pulsar’s initial period and P_∞ is its limiting period as $t \rightarrow \infty$. Assuming that pulsars eventually slow substantially from their initial spin period, $P_0 \ll P_\infty$, we can approximate equation (6) by

$$P(t) \approx P_\infty [1 - \exp(-2t/\tau)]^{1/(n-1)}. \quad (7)$$

Using (7) for $P(t)$ in (4) for $\rho(t)$ yields a simple approximation for the evolution of ρ , expressed directly in terms of t :

$$\rho(t) \approx \rho_\infty [1 - \exp(-2t/\tau)]^{-\gamma/(n-1)}, \quad (8)$$

where ρ_∞ is the limiting emission cone half-angle as $t \rightarrow \infty$.

We note that, because P_0 has effectively been taken as zero in going from (6) to (7) for $P(t)$, equation (8) is not applicable to the very youngest pulsars: for $t \ll \tau/2$ it reduces to

$$\rho(t)/\rho_\infty \approx (\tau/2t)^{\gamma/(n-1)}, \quad (9)$$

which diverges as $t \rightarrow 0$. For the typical parameter values (see Section 4.3 Table 3) $\gamma = 1/2$, $n = 2.3$, $\tau = 1 \times 10^6$ yr, and $\rho_\infty = 2 - 5^\circ$, equation (9) gives $\rho(t) \approx 11\rho_\infty \approx 22 - 55^\circ$ for $t \approx 1000$ yr. As only one known pulsar is this young, the divergence is outside the age range we can analyse, and the approximation (8) for $\rho(t)$ is valid for our purposes.

2.2 Evolution in characteristic age

A pulsar’s spin-down age, $t_s \equiv P/[(n-1)\dot{P}]$, depends on n , which is going to be a variable in our fitting procedure below. Instead of the spin-down age, from here on we use the characteristic age which is defined to be

$$t_c \equiv P/(2\dot{P}). \quad (10)$$

The characteristic age is independent of n and corresponds to the spin-down age in the case $n = 3$. Its use enables us to show fittings for different n on one plot using the same characteristic-age data. Inserting equation (7) for $P(t)$, we find that t_c is related to the pulsar’s actual age, t , by:

$$t_c(t)/\tau = [(n-1)/4][\exp(2t/\tau) - 1] \quad (11)$$

$$\text{or } \exp[2t(t_c)/\tau] = 1 + (4t_c)/(n-1)\tau. \quad (12)$$

Note that factors of $2/(n-1)$ effectively rescale t_c to t_s in these equations.

¹ <http://www.atnf.csiro.au/research/pulsar/psrcat/>

It follows from equation (11) that $t_c \approx (n-1)t/2$ for relatively young pulsars (young compared with the spin-down time-scale); for old pulsars, t_c/τ increases as an exponential function of t/τ . The characteristic and actual ages coincide for relatively young pulsars in the dipole rotator case, for which $n = 3$.

The t_c - t relation enables equations (3), (7) and (8) for α , P and ρ to be re-expressed in terms of t_c – which has the advantage of being directly determined from the measured quantities P and \dot{P} – instead of in terms of t :

$$\sin \alpha(t_c) = (\sin \alpha_0) [1 + 4t_c/(n-1)\tau]^{-1/2}, \quad (13)$$

$$P(t_c) = P_\infty [1 + (n-1)\tau/4t_c]^{-1/(n-1)}, \quad (14)$$

$$\text{and } \rho(t_c) = \rho_\infty [1 + (n-1)\tau/4t_c]^{\gamma/(n-1)}. \quad (15)$$

Equation (15) describes an emission-cone half-width that decreases quite rapidly with time for young pulsars; consequently, the observed pulsewidths should decrease with age for the youngest pulsars. The alignment of the spin and magnetic axes, described by equation (13), should cause an increase in the observed pulsewidths for older pulsars, as the pulse will occupy a larger fraction of a complete rotation. The combination of these two processes should lead to a minimum in the observed angular pulsewidths for pulsars of moderate ages (CB83).

Note that taking the derivative of equation (6) and using equation (10) for t_c gives (cf. equation (2))

$$n_{\text{app}} = n + 4t_c/\tau, \quad (16)$$

showing that the apparent braking index increases with characteristic age.

2.3 The parameters of the theory

Equations (13), (14) and (15) – expressing the evolution of the magnetic-spin inclination angle, the pulsar period and the emission cone half-angle in terms of a pulsar's characteristic age – can conveniently be re-written in terms of a normalized dimensionless characteristic age:

$$T_c \equiv 2t_c/[(n-1)\tau], \quad (17)$$

which reduces to t_c/τ in the dipole rotator ($n = 3$) case. Thus:

$$\sin \alpha(T_c) = (\sin \alpha_0) (1 + 2T_c)^{-1/2}, \quad (18)$$

$$P(T_c) = P_\infty [1 + (2T_c)^{-1}]^{-1/(n-1)}, \quad (19)$$

$$\text{and } \rho(T_c) = \rho_\infty [1 + (2T_c)^{-1}]^{\gamma/(n-1)}. \quad (20)$$

In the equations used for the pulsewidth modelling below, namely (13) and (15), or (18) and (20), for $\alpha(t_c)$ and $\rho(t_c)$, n appears only in the two combinations $\gamma/(n-1)$ and $(n-1)\tau$. Hence there are only four basic independent parameters in the Candy-Blair alignment models. Later we will set $\gamma = 1/2$, consistent with the γ values found by other authors (e.g. Rankin 1993a; McKinnon 1993; Gould 1994). Hence, it is convenient in this study to define the four independent parameters to be α_0 , ρ_∞ , n_γ and τ_γ , where

$$n_\gamma \equiv 1 + (n-1)/(2\gamma), \quad \text{and} \quad (21)$$

$$\tau_\gamma \equiv 2\gamma\tau, \quad (22)$$

since these last two parameters are normalized to the $\gamma = 1/2$ case. In terms of these parameters, the two combinations $\gamma/(n-1)$ and $(n-1)\tau$ become

$$\gamma/(n-1) = 1/[2(n_\gamma - 1)], \quad \text{and} \quad (23)$$

$$(n-1)\tau = (n_\gamma - 1)\tau_\gamma, \quad (24)$$

and equation (16) gives

$$n_{\text{app}} - 1 = 2\gamma \left(n_\gamma - 1 + \frac{t_c}{\tau_\gamma} \right). \quad (25)$$

3 PULSEWIDTH EVOLUTION DESCRIPTION

3.1 Mean pulsewidths

For an individual pulsar, the observed angular pulsewidth is given as a function of α , ρ and ζ by

$$W(\alpha, \rho, \zeta) = 2 \arccos \left(\frac{\cos \rho - \cos \alpha \cos \zeta}{\sin \alpha \sin \zeta} \right), \quad (26)$$

where ζ is the angle between the observer's direction and the pulsar's spin axis (Manchester & Taylor 1977, p. 218). The strong dependence on the orientation of the observer with respect to the spin axis leads to a wide scatter in the pulsewidth values, so we need to take a mean pulsewidth for pulsars with certain values of α and ρ .

The mean pulsewidth is obtained by integrating (26) over the angular extent of the emission beam:

$$\langle W \rangle(\alpha, \rho) = \int_{|\alpha-\rho|}^{\alpha+\rho} W(\alpha, \rho, \zeta) P(\zeta) d\zeta, \quad (27)$$

in which $P(\zeta)d\zeta$ is the probability that the angle between the spin axis and the observer's direction is in the range ζ to $\zeta + d\zeta$. The integration is over all angles ζ for which emission is both directed toward the observer and seen as pulsed.

The limits of integration in (27) for $\langle W \rangle(\alpha, \rho)$ are explained by means of Fig. 1. For a pulsar that is not too close to alignment, such that the emission beam does not contain the rotation axis (Fig. 1, left), $\alpha > \rho$ and the beam is intercepted for a part (but not all) of the rotation period if ζ is in the range $\alpha - \rho$ to $\alpha + \rho$. For a pulsar that is close to alignment, with the emission beam containing the rotation axis (Fig. 1, right), $\alpha < \rho$ and the range $\zeta < \rho - \alpha$ is excluded, as some part of the beam is then always directed toward the observer, assuming the emission cone to be filled.

We take $\alpha \leq 90^\circ$; the choice of first or second quadrant for α is a matter of convention, switching it between hemispheres being equivalent to reversing the sense of the neutron star's rotation. The beam, however, can extend into the other hemisphere, which it will do if $\alpha + \rho > \pi/2$, as expected for young pulsars with wide beams. If a pulsar produces observable radio emission from both poles, then this will be observed as a main pulse and interpulse, provided that the pulsar is nearly orthogonal or the pulsar beams are wide. However, the mean pulsewidths referred to here are for emission from only one of these poles, not the combined main pulse – interpulse width.

On taking pulsar spin axes to be randomly directed with respect to observers, and normalizing over the angular extent of the emission cone, the probability distribution for ζ becomes:

$$P(\zeta)d\zeta = (\sin \zeta d\zeta/2)/f_b(\alpha, \rho), \quad (28)$$

where f_b is the 'beaming fraction', which measures the fraction of the sky swept out by the beam. Equation (28) is the ratio of the surface area of a ring on a sphere, corresponding to observers in the range ζ to $\zeta + d\zeta$, to the surface area of the sphere swept out by the beam.

The surface area of the part of a sphere between co-latitudes θ_1 and θ_2 , normalized to the surface area of a sphere, is

$$\sin [(\theta_1 + \theta_2)/2] \sin [(\theta_2 - \theta_1)/2]. \quad (29)$$

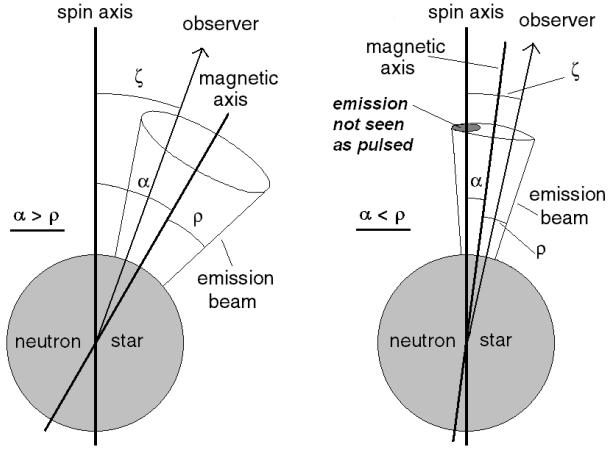


Figure 1. Pulsar emission relative to a distant observer, assuming a circular cone of emitted radiation, with the magnetic-spin inclination angle α either greater (left) or less (right) than the emission cone half-angle ρ . In the latter case, the emission cone encloses the spin axis, and there may be little or no modulation; in particular, to observers in the cone $\zeta < \rho - \alpha$, the emission cone is continuously visible. The left-hand diagram depicts the usual case of a pulsar with moderate values of α and ρ , typical of mature-aged pulsars. The right-hand diagram depicts a pulsar with a thin beam and nearly aligned spin and magnetic axes, typical of old pulsars in the Candy-Blair theory and the Jones model.

Inserting $\theta_1 = |\alpha - \rho|$ and $\theta_2 = \alpha + \rho$ gives the beaming fraction:

$$f_b(\alpha, \rho) = \sin \alpha \sin \rho, \quad (30)$$

applicable to both situations depicted in Fig. 1.

We note that Tauris & Manchester (1998, eq. (7)) use a different beaming fraction for the case $\alpha < \rho$, namely $1 - \cos(\alpha + \rho)$, which results from integration over 0 to $\alpha + \rho$. As they remark, there may be little or no modulation when $\alpha < \rho$, and we prefer to exclude the ‘continuously seen’ cone, $\zeta < \rho - \alpha$ (Fig. 1, right).

3.2 Evolution modelling

The evolutionary time dependence of α and ρ , equations (3) and (8), results in a mean pulsewidth, $\langle W \rangle(\alpha, \rho)$, that is a function of time only, $\langle W \rangle(t)$. This function is to be treated as a density, $\langle W \rangle(t) dt$ giving the mean pulsewidth of pulsars aged between t and $t + dt$. The age of the pulsars will here be measured in terms of their log characteristic age, $\log t_c$, and will be binned with respect to that variable. Under the change of variables $t \rightarrow t(\log t_c)$, we have

$$\langle W \rangle(t) dt = \langle W \rangle(t(\log t_c)) \frac{dt}{d(\log t_c)} d(\log t_c) \quad (31)$$

$$\equiv \langle W \rangle(\log t_c) f_t d(\log t_c). \quad (32)$$

The factor $f_t(t_c)$ is given by

$$f_t \equiv \frac{dt}{d \log t_c} = \frac{\tau \ln 10}{2} \left(1 + \frac{(n-1)\tau}{4t_c} \right)^{-1}, \quad (33)$$

where the $t-t_c$ relation, equation (12), has been used. So $f_t(t_c)$ increases monotonically from $(\ln 10)2t_c/(n-1)$ for young pulsars, flattening to $(\ln 10)\tau/2$ for old ones.

To allow for variations between the evolutionary histories of different pulsars, CB86 and C93 relaxed the assumptions that all pulsars are born with the same inclination angle and have the same

alignment time-scale, α_0 and τ respectively. Instead, these are replaced by a probability distribution function, $P(\alpha_0)$, for initial inclination angles (see Section 3.3), and a log-normal distribution of alignment time-scales:

$$P(\log \tau) = \frac{1}{\sqrt{2\pi}\sigma_{\log}} \exp \left[-\frac{1}{2} \left(\frac{\log \tau - \mu_{\log}}{\sigma_{\log}} \right)^2 \right], \quad (34)$$

where μ_{\log} and σ_{\log} are the mean and standard deviation of the logarithm of the time-scale distribution, $\log \tau$. If the normalized parameters n_γ and τ_γ that were introduced in equations (21)–(24) are used, then τ_γ has a log-normal distribution with mean

$$\mu_{\gamma, \log} = \mu_{\log} + \log(2\gamma) \quad (35)$$

and standard deviation σ_{\log} unchanged.

The mean observed pulsewidth as a function of characteristic age is now given by

$$\langle W \rangle(\log t_c) = \frac{1}{A} \int_0^\infty \int_0^{\pi/2} \langle W \rangle(\alpha, \rho) f_b f_t P(\alpha_0) P(\log \tau) d\alpha_0 \frac{d\tau}{\tau}, \quad (36)$$

in which the normalization factor, A , is

$$A(\log t_c) = \int_0^\infty \int_0^{\pi/2} f_b f_t P(\alpha_0) P(\log \tau) d\alpha_0 \frac{d\tau}{\tau}. \quad (37)$$

The beaming fraction, f_b , must be included as a weighting factor in equation (36) to take into account the effect of beaming on the probability of observation, and those weights are normalized by the factor A^{-1} (the mean pulsewidth is only computed for those pulsars that are observed). The aim here is to fit equation (36) for $\langle W \rangle(\log t_c)$ to the observed data.

In Appendix A it is shown that

$$\langle W \rangle(\alpha, \rho) f_b = \begin{cases} [1 - \cos \rho] \pi & \text{for } \alpha \geq \rho, \\ [\cos(\rho - \alpha) - \cos \rho] \pi & \text{for } \alpha \leq \rho. \end{cases} \quad (38)$$

Inserting this result into equation (36) for $\langle W \rangle(\log t_c)$ allows a considerable improvement in the numerical performance of the curve-fitting.

At a given characteristic age, Equation (15) implies that $\rho(t_c) > 90^\circ$ if a pulsar were to have $\tau > \tau_{\text{cut}}$, where

$$\tau_{\text{cut}}(t_c) \equiv \frac{4t_c}{n-1} \left[\left(\frac{90^\circ}{\rho_\infty} \right)^{(n-1)/\gamma} - 1 \right] \quad (39)$$

$$\approx \frac{4t_c}{n-1} \left(\frac{90^\circ}{\rho_\infty} \right)^{\frac{n-1}{\gamma}}, \text{ for } \rho_\infty \ll 90^\circ. \quad (40)$$

This unphysical possibility arises from the approximation made earlier that $P_0/P_\infty \rightarrow 0$. In reality a pulsar with $\tau > \tau_{\text{cut}}$ must be born with a characteristic age greater than the t_c used in equation (39). Therefore integrals over τ are terminated at an upper limit of $0.99\tau_{\text{cut}}$, where the factor 0.99 is included to assist numerical convergence.

3.3 Three initial alignment models

We use three different initial alignment models, $P(\alpha_0)$, from C93 that involve different distributions of the initial inclination angles. Model I assumes that all pulsars start with their spin and magnetic axes mutually perpendicular: $\alpha_0 = 90^\circ$. This corresponds to the

Jones model following the initial brief phase of counter-alignment to orthogonality. Model II uses the probability distribution

$$P(\alpha_0) = (2 - \sqrt{2})^{-1} \sin(\alpha_0/2), \quad (41)$$

which assumes pulsars are born with a random distribution of inclination angles from 0 to 90°. Model III uses

$$P(\alpha_0) = (4/\pi) \cos^2 \alpha_0, \quad (42)$$

which assumes pulsars tend to be born with inclination angles closer to 0 than would occur by chance. At the outset there is no particular reason to think that Model III might be approximately correct; it is included here for contrast with Models I and II.

4 FITTING TO DATA

4.1 Data selection

Both 10 per cent and 50 per cent intensity pulsewidth data, W_{10} and W_{50} , are used in this analysis of pulsewidth evolution. The data were retrieved from the ATNF pulsar catalogue (Manchester et al. 2005), which includes results from several surveys at around 400 and 1400 MHz. For this study, all the binary, millisecond, anomalous X-ray, rotating radio transient (RRAT) and globular cluster pulsars have been removed from the data set, because these pulsars are considered to follow different evolutionary histories from those of the more common isolated radio pulsars. The condition for excluding millisecond (or low magnetic field) pulsars was chosen to be $B_{\text{surf}} \leq 4 \times 10^9$ G.

Pulsars with interpsuls whose W_{10} or W_{50} values potentially include both the main pulse and interpulse were also removed. To do this the complete census of the interpulse pulsar population recently published by Weltevrede & Johnston (2008) was used. It identified 27 pulsars with interpsuls, and our Fig. 2 shows histograms of the existing W_{10} and W_{50} values for them: it is evident that the distributions can be treated as bimodal with one maximum well below 90° and the other at around 180°. For the purposes of this study it was assumed that a value of W_{10} or $W_{50} > 140^\circ$ includes emission from both poles of the pulsar (that is both the main pulse and the interpulse), and so should not be included in the study. This resulted in 6 pulsars being removed from the W_{10} data set leaving a net total of 872 pulsars; and 3 interpulse pulsars being removed from the W_{50} data set, leaving a net total of 1420 pulsars. These two data sets are referred to hereafter as ‘ATNF Cat W_{10} ’ and ‘ATNF Cat W_{50} ’.

In a mean pulse profile the spacing between components usually increases, and with it the whole profile width, as the radio frequency, f , decreases. For instance, by measuring the profile widths of 6 pulsars up to 32 GHz, Xilouris et al. (1996) found that $W_{50} = b_0 + b_1 f^{-p}$ where p , b_0 and b_1 are constant for each pulsar, with $0.3 < p < 0.9$. The W_{10} and W_{50} pulsewidths tabulated in the ATNF catalogue are not all measured at the same observing frequency. The frequency dependence of the pulsewidth therefore introduces some statistical noise into the ‘ATNF Cat W_{10} ’ and ‘ATNF Cat W_{50} ’ data sets. As a consistency check, we have also examined the subsets consisting of only those pulsars whose catalogued pulsewidth values were measured in the Parkes Multibeam Survey at 1374 MHz (Manchester et al. 2001; Lorimer et al. 2006). These subsets are referred to hereafter as ‘Parkes MB W_{10} ’ and ‘Parkes MB W_{50} ’, and contain 377 and 934 pulsars respectively.

Both the W_{10} and W_{50} characteristic age–pulsewidth data distributions naturally lend themselves to binning in $\log t_c$, and it was

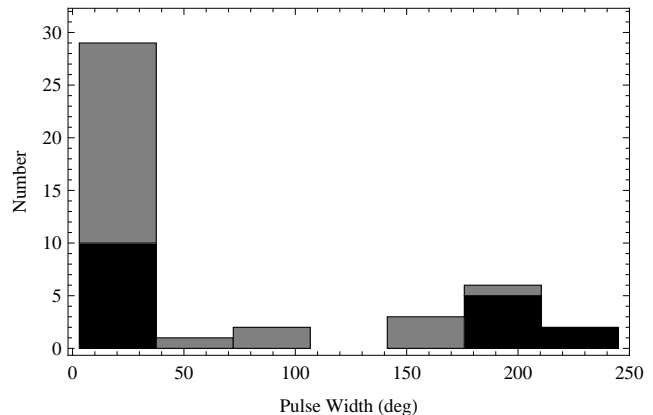


Figure 2. Frequency histograms of the W_{10} (black) and W_{50} (grey) pulsewidths for the interpulse pulsars listed by Weltevrede & Johnston (2008); the bars are stacked for clarity. It is evident that the data distributions can be treated as bimodal. Widths greater than 140° were assumed to have included the interpsuls and were excluded from the W_{10} and W_{50} pulsewidth data sets used in this paper.

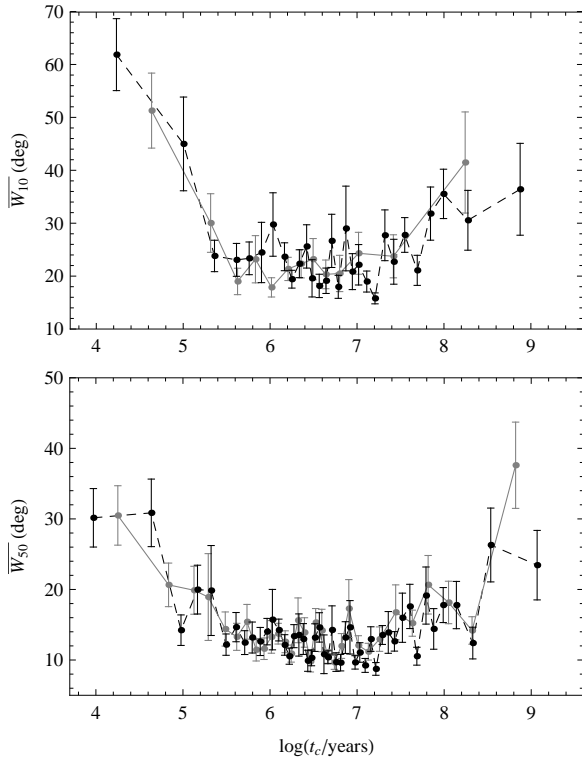
also found numerically optimal to fit the mean pulsewidth, equation (36), as a function of $\log t_c$ rather than t_c , i.e. as $\langle W \rangle(\log t_c)$. The W_{10} or W_{50} data set is then binned to give N data points, $\{(\log t_c)_i, \overline{W}_i\}$, $i = 1, \dots, N$. It is desirable to make the bins as narrow as possible in order to give maximum resolution in $\log t_c$. This is because if a bin i extends over a large range of $\log t_c$ in a region where the underlying function, here $\langle W \rangle(\log t_c)$, has a significant slope, then a part of the uncertainty in the estimated value of the mean pulsewidth, \overline{W}_i , will result from the change in the underlying $\langle W \rangle(\log t_c)$ across the bin. On the other hand, it is desirable to include as many points as possible in a bin to reduce the uncertainty in the \overline{W}_i estimate of $\langle W \rangle[(\log t_c)_i]$, and also to ensure that the errors in the estimates are approximately normally distributed so that standard data-analysis procedures can be applied. To attempt to balance these competing effects we binned the data so that each bin contained about 30 pulsars – the minimum number of points to ensure that the errors are approximately normally distributed.

Least-squares fittings are made to both the W_{10} and W_{50} data sets. Even though there are more data points in the W_{50} than the W_{10} data sets, the W_{10} is superior for our pulsewidth fitting because the W_{50} set suffers more from confusion. This is because a W_{50} measurement will include outlying components in a profile only if they are above 50 per cent of the maximum intensity. A W_{10} measurement is more likely to include the outlying components and so will give a more consistent estimate of the total pulsewidth. A histogram of the ratio of W_{10}/W_{50} is found to be unimodal, with a peak at about 2. However, it extends to ratios above 10, demonstrating that the W_{10} in those cases is detecting outlying emission missed by the W_{50} measurement. The trade-off in relying on W_{10} values is that the W_{10} measurement is more difficult to make than the W_{50} , and so there are fewer pulsars with existing W_{10} measurements.

The data sets considered in this paper are summarized in Table 1. For each data set it gives the name of the set and the number of pulsars it contains, and describes the binning of the data. Fig. 3 shows the ATNF Cat data sets and compares them to the corresponding Parkes MB data sets. We see that the ATNF Cat and Parkes MB data sets have very similar distributions with respect to characteristic age.

Table 1. Summary of the four data sets considered in this paper.

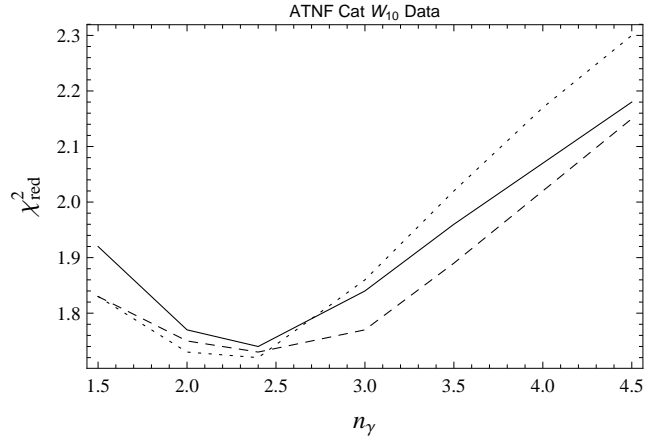
Dataset	Size	Binning
Parkes MB W_{10}	377	bins 1–13: 29 pulsars/bin
Parkes MB W_{50}	934	bins 1–14, 19–31: 30 pulsars/bin
ATNF Cat W_{10}	872	bins 15–18: 31 pulsars/bin bins 1–14, 17–29: 30 pulsars/bin
ANTF Cat W_{50}	1420	bins 15–16: 31 pulsars/bin bins 1–19, 30–47: 30 pulsars/bin bins 20–29: 31 pulsars/bin

**Figure 3.** Comparison of the four mean-pulsewidth data sets considered in this paper, as summarized in Table 1. The W_{10} and W_{50} ‘ATNF Cat’ data sets are shown in black (connected by a dashed black line), while the two corresponding ‘Parkes MB’ data sets are shown in grey (connected by a solid grey line). The error bars are 1σ standard errors for the binned data.

4.2 Fitting procedure

Each model of initial alignment has four free parameters: ρ_∞ , n_γ , $\mu_{\gamma,\log}$ and σ_{\log} . The aim is to determine these four parameters by least-squares fitting the model $\langle W \rangle(\log t_c)$ -curve to the binned data. The mean pulsewidths, \overline{W}_i , computed for each bin i , have normally-distributed errors, and so the uncertainties for the fitted parameters can be found by computing the parameter covariance matrix, s_{kl} (e.g. Press et al. 1992, Ch. 15). This matrix can in turn be used to compute a parameter correlation matrix, r_{kl} , for the parameter estimates.

Proceeding in this way it was found that least-squares estimates of the four parameters had large uncertainties, and hence were of questionable statistical merit. These large uncertainties were found to result mostly from a high correlation between the four parameters, with the off-diagonal values of the parameter cor-

**Figure 4.** Plot of χ_{red}^2 as a function of n_γ , for each of the three models of initial alignment fitted to the ATNF Cat W_{10} data: Model I (solid black), Model II (dashed), and Model III (dotted). Each model exhibits a minimum in χ_{red}^2 at n_γ around 2.3.

relation matrix all being around ± 0.98 . Furthermore, very different sets of parameter values could give very similar fittings to the data.

To tackle these problems we fixed n_γ at specific trial values, leaving three free parameters: ρ_∞ , $\mu_{\gamma,\log}$, and σ_{\log} . The cross-correlation between the parameters was significantly reduced. Correspondingly, the uncertainties in the parameters were also significantly reduced and, given the assumptions, provided statistically significant constraints. The reduced χ^2 ($\chi_{\text{red}}^2 \equiv \chi^2/\text{dof}$) for these three-parameter fits were then examined as a function of the pre-set parameter n_γ ; a minimum in this function would indicate that a particular value of n_γ was giving a superior fit. In that case a least-squares fit was computed by allowing all four parameters (including n_γ) to vary, and the solution was checked against the three-parameter fit for consistency.

We recall that the parameters n_γ and $\mu_{\gamma,\log}$ are the values of n and μ_{\log} assuming that $\gamma = 1/2$. More generally, for fitted values of n_γ and $\mu_{\gamma,\log}$, the relationships between different values γ , n and μ_{\log} are found via equations (21) and (35) to be $n = 2\gamma(n_\gamma - 1) + 1$, $\mu_{\log} = \mu_{\gamma,\log} - \log(2\gamma)$, and hence

$$\frac{n-1}{n_\gamma-1} = 10^{\mu_{\gamma,\log} - \mu_{\log}}. \quad (43)$$

4.3 Fits to the data

The three-parameter fits showed clear minima in $\chi_{\text{red}}^2(n_\gamma)$ at $n_\gamma \approx 2.3$ for all of the datasets, excluding the ATNF Cat W_{50} data. For instance, Fig. 4 plots $\chi_{\text{red}}^2(n_\gamma)$ for Models I, II and III fitted to the ATNF Cat W_{10} data.

Fig. 5 shows three-parameter fitted curves of $\langle W \rangle(\log t_c)$ for Model II with n_γ set at values between 1.5 and 4; equivalent plots for Models I and III are similar. In each case setting n_γ to around 2.3 and least-squares fitting the other three parameters gives the best fit to the data, in particular at low characteristic age. Performing the same procedure with n_γ higher or lower than this value results in a curve that goes to lower pulsewidth than the measured value at low $\log t_c$. The figure shows for the ATNF Cat W_{50} data set that even though χ_{red}^2 does not have a clear minimum at $n_\gamma \approx 2.3$, the $n_\gamma \approx 2.3$ fit appears to best explain the low- t_c mean W_{50} pulsewidths.

Table 2 gives the measured values of n_{app} for six pulsars (ta-

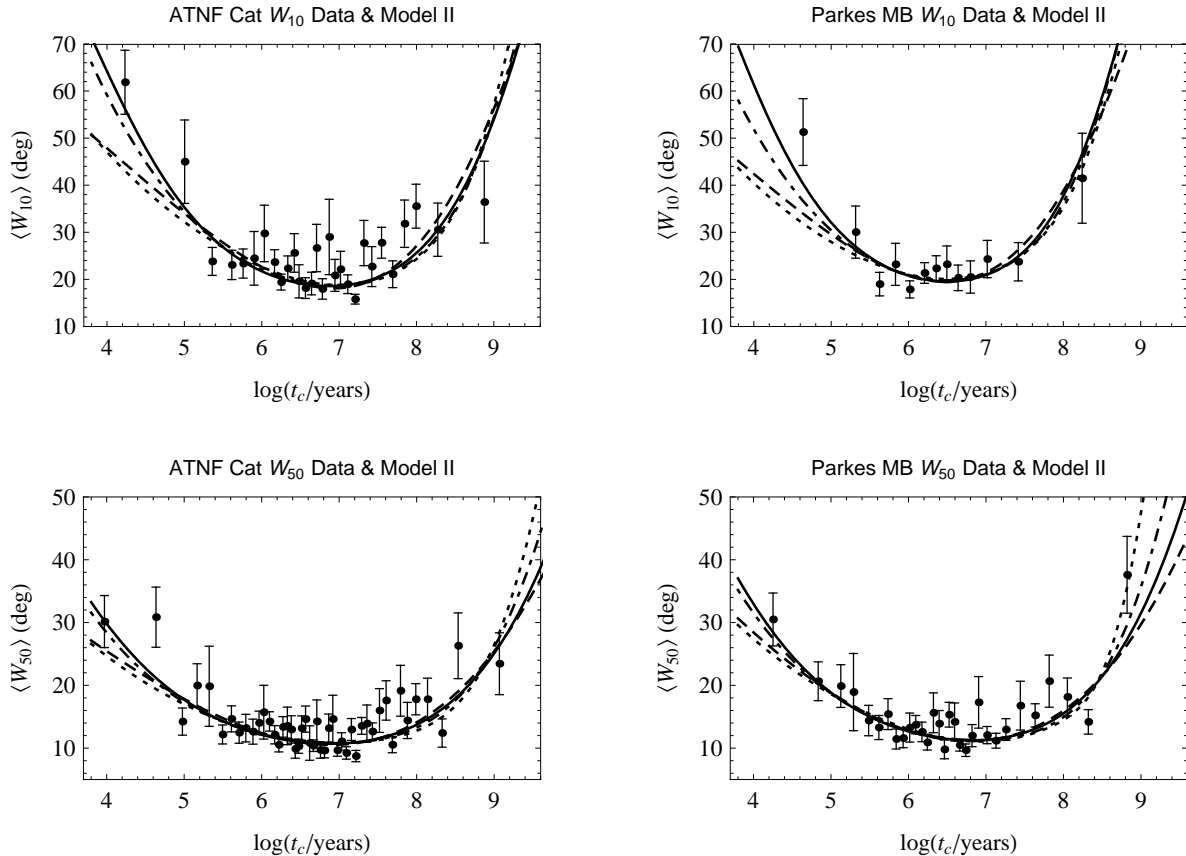


Figure 5. Mean pulsewidth, $\langle W \rangle$, as a function of log characteristic age. The data sets are given in the title of each figure; they are the same as those plotted in Fig. 3 and are summarized in Table 1. Error bars are 1σ standard errors for the binned data. Mean angular pulsewidths for Model II are least-squares fitted to the binned data for each of the following values of n_γ : $n_\gamma = 1.5$ (dashed), $n_\gamma = 2.3$ (solid), $n_\gamma = 3.0$ (dot-dashed), and $n_\gamma = 4$ (dotted). The vertical scales are different for the W_{10} and W_{50} data sets. Note that for the Parkes MB W_{50} data set, the Model II curves did not converge for $n_\gamma = 1.5$ or $n_\gamma \geq 4$. In that case, the dashed curve and the dotted curve represent $n_\gamma = 1.7$ and 3.95 respectively. In each plot, except the ATNF Cat W_{50} plot, the solid $n_\gamma = 2.3$ curve is approximately the best-fitting curve to the data across the different values of n_γ , having the lowest value of χ_{red}^2 . None of the curves in the ATNF Cat W_{50} plot was clearly distinguished by a minimum in χ_{red}^2 .

ble 2, p. 1291, Livingstone et al. 2006, and references therein). The uncertainties in the last digit of n_{app} are shown, being 1σ confidence intervals. The characteristic ages are also listed, indicating that these pulsars are all very young. Except for the Vela pulsar, the determinations of n_{app} were all made by standard timing analyses that obtained phase coherent solutions (Livingstone et al. 2007). This approach could not be used for the Vela pulsar because of its large glitches, so $\dot{\nu}$ was determined from data 150 days after each glitch and then extrapolated back to the glitch epoch; $\dot{\nu}$ could then be determined from the change in $\dot{\nu}$ over time (Lyne et al. 1996).

It is noteworthy that the mean value of n_{app} in Table 2 is 2.42 ± 0.05 , compared to the values of $n_\gamma \approx 2.3$ that give the best fits of the Candy-Blair models to the pulsewidth data. On the grounds of equation (25) we expect $n_{\text{app}} \approx n_\gamma$ for $\gamma \approx 1/2$ and $t_c \ll \tau_\gamma$. Fig. 5 shows that the constraint of $n_\gamma \approx 2.3$ is based primarily on young pulsars, but a much larger sample than the six given in Table 2.

Table 3 gives the parameter values obtained from the three-parameter fits to the four data sets. The error ranges are 1σ confidence intervals, and the degrees of freedom (dof) for each data set are given. For each fitting the parameter n_γ is fixed at the value at

Table 2. Measured values of the apparent braking index, n_{app} .

Pulsar	t_c (yr)	n_{app}	Reference
J1846-0258	723	2.65(1)	Livingstone et al. (2006)
B0531+21, Crab	1240	2.51(1)	Lyne et al. (1993)
B1509-58	1550	2.839(3)	Livingstone et al. (2005)
J1119-6127	1610	2.91(5)	Camilo et al. (2000)
B0540-69, LMC	1670	2.140(9)	Livingstone et al. (2005)
B0833-45, Vela	11300	1.4(2)	Lyne et al. (1996)

which χ_{red}^2 is minimum, except in the case of the ATNF Cat W_{50} data where no clear minima were found, and so n_γ was fixed at 2.3 for comparison with the other fits. For each data set, all three models predict similar $\mu_{\gamma, \log}$ and σ_{\log} values. The only significant parameter difference between the three alignment models is the predicted limiting emission cone half-width, ρ_∞ . Fig. 6 shows curves of $\langle W \rangle(\log t_c)$ for Models I, II and III using the parameter values listed in Table 3. It is evident that the pulsewidth data alone can not be used to distinguish between the three models of initial alignment.

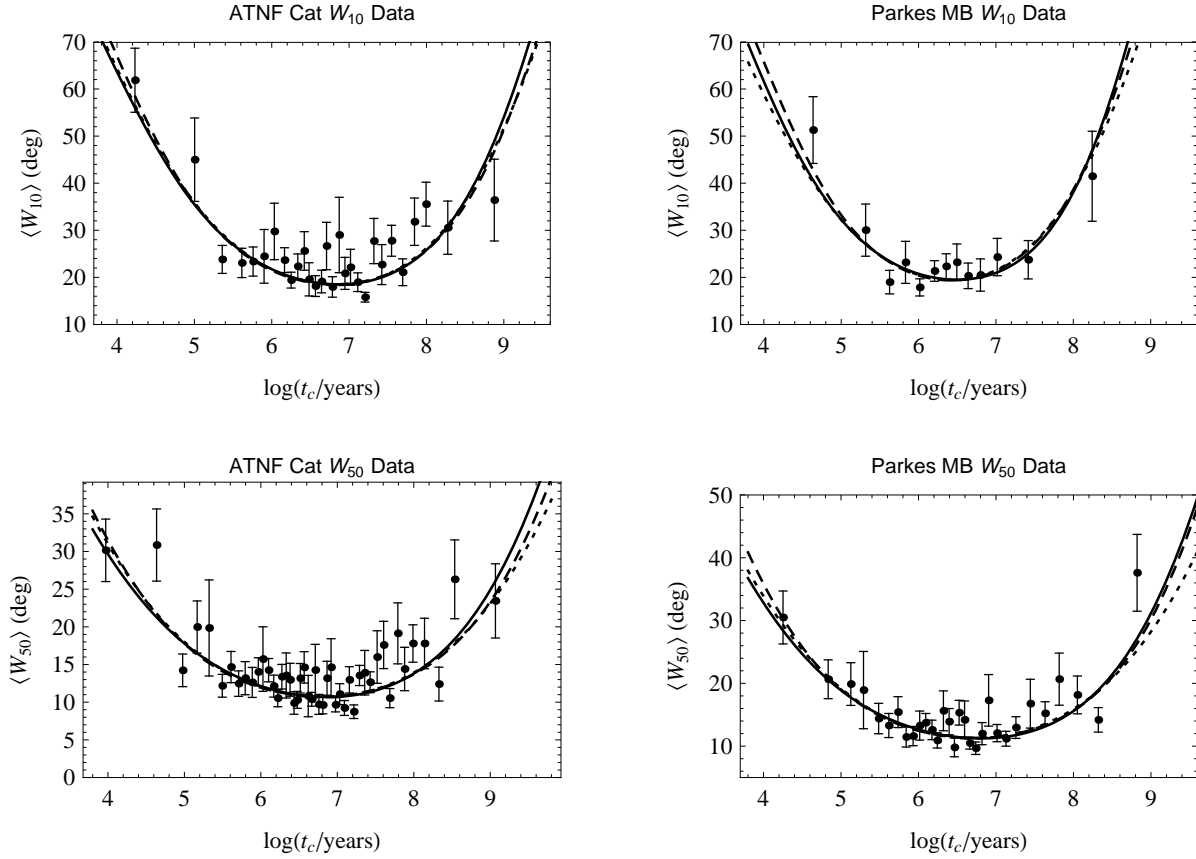


Figure 6. Mean pulsewidth, $\langle W \rangle$, as a function of log characteristic age using the fitting parameters given in Table 3. Mean angular pulsewidths for Models I (dashed line), II (solid) and III (dotted) are least-squares fitted to the binned data.

The figures show that following a rapid decline in pulsewidth for young pulsars, there is a minimum in the pulsewidth for pulsars of moderate age followed by an increase for older pulsars: this is a clear signature of spin-magnetic alignment (CB83). The minimum occurs at $t_c \approx 10^{6.9}$ yr in all three models for all data sets, except the Parkes MB W_{10} data set where it occurs slightly earlier. The mean alignment time-scales obtained from the fitting process are around 10^6 yr which is less than previous estimates of around 10^7 yr. The log deviations of the time-scales range from 0.71 to 1.21, and are all larger than the value of 0.25 found by both CB86 and C93, which suggests that the more sensitive recent surveys have detected pulsars with a broader range of parameters.

As discussed near the end of Section 4.1, W_{10} is superior to W_{50} for pulsewidth fitting. Hence in the following we restrict our attention to the W_{10} fits, in particular the ATNF Cat W_{10} fit that was generated from a larger data set.

5 ANALYSIS AND IMPLICATIONS

5.1 Magnetic field decay model

As an alternative to magnetic alignment, many authors have proposed pulsar evolution through magnetic field decay. This will have a different effect on pulsewidth evolution. Suppose that the magnetic field decays exponentially, according to

$$B = B_0 \exp(-t/\tau_d), \quad (44)$$

where τ_d is the field decay time-scale, and that $\alpha = \alpha_0$ remains constant (no alignment). Equation (5) for $P(t)$ still applies, so we still have equations (8) and (15) for $\rho(t)$ and $\rho(t_c)$.

Fig. 7 shows curves of $\langle W \rangle(\log t_c)$ for a constant $\alpha = \alpha_0$ (using Models I, II and III for the α_0 distribution) to illustrate the effect of magnetic field decay on pulsewidth evolution. The figure shows the same ATNF Cat W_{10} binned data as before and the curves have been fitted assuming that $\log \tau_d$ has a normal distribution with mean μ_d and standard deviation σ_d . It was found necessary to fix σ_d in order to get a convergent fit, and the small value of $\sigma_d = 0.1$ was required in order to increase the size of μ_d to realistic values.

Qualitatively, the effect of field decay alone on pulsewidth evolution is a progressive decrease in pulsewidth over time, as seen in Fig. 7. The data do not support this evolution path: in contrast to the alignment models, the field decay model does not account for the increase in pulsewidth values for older pulsars.

From this work we cannot set an upper limit on the magnetic field decay rate. Clearly, weak magnetic-field decay could still occur concurrently with the alignment mechanism that causes the observed increase in pulsewidth for old pulsars. We can say that magnetic field decay is not the dominant evolutionary factor: both the W_{50} and W_{10} fits are consistent with magnetic field decay not being a significant factor in pulsar evolution. To model the combined

Table 3. Three-parameter least-squares fits of Models I, II and III.

	n_γ	ρ_∞ (deg)	$\mu_{\gamma,\log}$	σ_{\log}	χ^2_{red}
ATNF Cat W_{10} Fits (dof = 26)					
I	2.47	5.6 ± 0.2	6.5 ± 0.2	0.71 ± 0.08	1.73
II	2.30	4.11 ± 0.12	6.1 ± 0.2	0.83 ± 0.08	1.74
III	2.25	1.99 ± 0.08	6.2 ± 0.3	0.89 ± 0.08	1.72
ATNF Cat W_{50} Fits (dof = 44)					
$n_\gamma \equiv 2.3$ (no clear minimum in χ^2_{red})					
I	2.3	2.78 ± 0.08	5.4 ± 0.3	1.02 ± 0.08	1.47
II	2.3	2.10 ± 0.07	4.8 ± 0.4	1.20 ± 0.08	1.46
III	2.3	0.87 ± 0.04	5.1 ± 0.4	1.26 ± 0.09	1.46
Parkes MB W_{10} Fits (dof = 10)					
I	2.19	5.5 ± 0.3	6.1 ± 0.4	0.66 ± 0.13	1.05
II	2.30	4.5 ± 0.2	6.1 ± 0.4	0.71 ± 0.14	1.18
III	2.05	1.84 ± 0.15	5.6 ± 0.5	0.90 ± 0.14	1.16
Parkes MB W_{50} Fits (dof = 28)					
I	2.48	3.33 ± 0.09	6.1 ± 0.3	0.83 ± 0.09	1.22
II	2.34	2.36 ± 0.08	5.3 ± 0.4	1.08 ± 0.09	1.25
III	2.20	0.87 ± 0.05	5.1 ± 0.4	1.21 ± 0.09	1.23

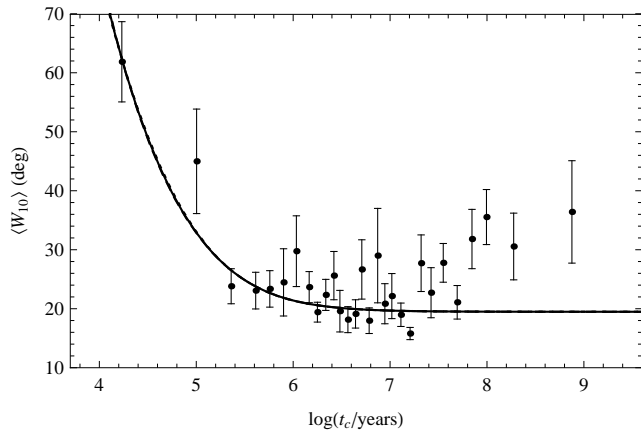


Figure 7. The mean angular pulsewidths obtained from the magnetic field decay model, as fitted to binned ATNF Cat W_{10} data, are plotted against characteristic age. It has been assumed here that each pulsar has a constant inclination angle, α_0 , with the distribution of those angles determined by either Model I (dashed), II (solid) or III (dotted) of inclination angle as outlined in Section 3.3; the three curves are indistinguishable.

effects of alignment and field decay is beyond the scope of this paper because of the relatively strong parameter cross-correlation that already exists in the alignment model alone.

5.2 Inclination angle evolution

To investigate the question of the alignment of the magnetic and spin axes, Tauris & Manchester (1998) used the data sets of Rankin (1993b) and Gould (1994) that give estimates of α for a few hundred pulsars. These two datasets are derived using slightly different methods and assumptions, as is well summarized by Tauris & Manchester (1998). Tauris & Manchester binned each data set in α to examine the $\langle \log t_c \rangle (\alpha)$ dependence. To these they fitted straight lines (their fig. 6, p. 632) in order to estimate the alignment time-scale, which they found to be around 10^7 yr.

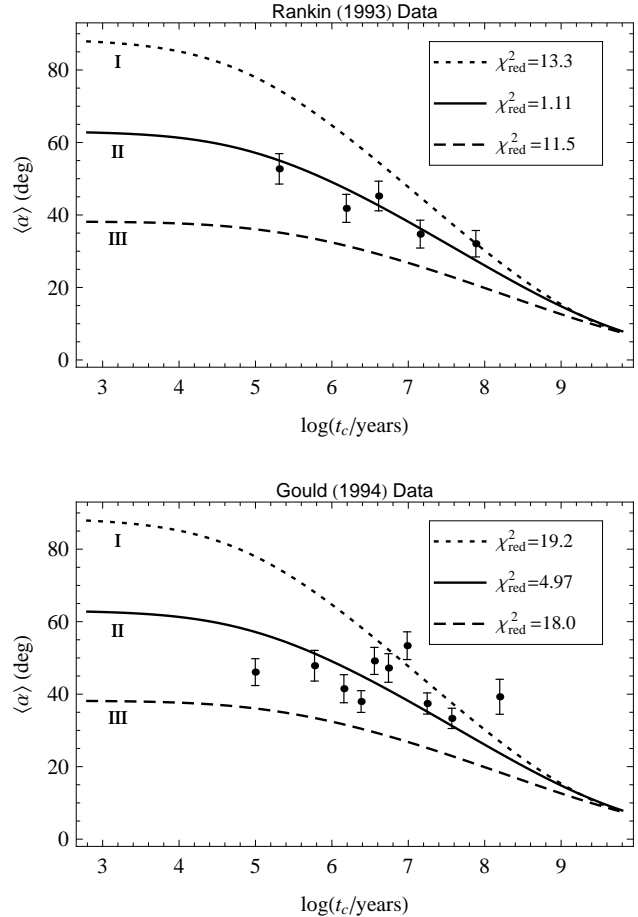


Figure 8. Mean angle of inclination, $\langle \alpha \rangle$, as a function of log characteristic age. The data are determined from models of beam morphology and polarization data and are taken from the two references considered by Tauris & Manchester (1998). Binned data are shown with 1σ error bars, and exclude low-field (millisecond) pulsars having $B_{\text{surf}} \leq 4 \times 10^9$ G. The top figure shows the Rankin (1993b, tables 2 and 4–8) inclination angles for 148 pulsars; the central 3 bins each contain 30 points, while the first and last bins contain 29. The bottom figure shows the Gould (1994, tables 1–6) inclination angles for 301 pulsars; of the 10 bins, all contain 30 points, except the sixth bin which has 31. The plotted curves are $\langle \alpha \rangle (\log t_c)$, equation (45), for each of the three models of initial alignment (I, II or III), using the parameter values determined from the best fits to the ATNF Cat W_{10} data. The goodness-of-fit of the model curves to the binned data is measured using the reduced chi-squared statistic, χ^2_{red} , and the values for each curve are shown on the plots. Models I and III are seen to give a poor fit to both the Rankin and Gould mean inclination-angle data, while Model II gives a particularly good fit to the Rankin data.

Conversely, here the mean inclination angle associated with a log characteristic age is found by averaging the arcsin of equation (13), for $\sin \alpha$, over the $P(\alpha_0)$ and $P(\log \tau)$ distributions:

$$\langle \alpha \rangle (\log t_c) = \frac{1}{A} \int_0^\infty \int_0^{\pi/2} \alpha (\log t_c) f_b f_t P(\alpha_0) P(\log \tau) d\alpha_0 \frac{d\tau}{\tau}. \quad (45)$$

Using the fitted-parameter values found in Section 4 from the various pulsewidth data sets, the resulting $\langle \alpha \rangle (\log t_c)$ curves for Models I, II and III are plotted in Fig. 8.

Also plotted are the data from Rankin (1993b) and Gould

(1994), in each case binned with about 30 points per bin. The error bars are 1σ standard errors computed from the binning. The actual errors in each of the α values are difficult to evaluate, since they depend on the validity of the underlying assumptions, as discussed by Manchester et al. (1998). As with the pulsewidth data, low-field (millisecond) pulsars having $B_{\text{surf}} \leq 4 \times 10^9$ G have been removed from the data.

The model curves are compared with the binned data using the reduced chi-squared statistic, χ_{red}^2 , which is shown for each model curve in Fig. 8. It was found that the inclination angle data are inconsistent with Models I and III, but compatible with Model II. Indeed Model II predicts the Rankin (1993b) data particularly well, with a $\chi_{\text{red}}^2 \sim 1$.

5.3 Beaming fraction evolution

From equations (13) and (15) for $\sin \alpha(t_c)$ and $\rho(t_c)$, equation (30) for f_b becomes

$$f_b(t_c) = \sin \alpha_0 [1 + 4t_c/(n-1)\tau]^{-1/2} \times \sin \left\{ \rho_\infty [1 + (n-1)\tau/4t_c]^{\gamma/(n-1)} \right\}. \quad (46)$$

The mean beaming fraction as a function of characteristic age, $\langle f_b \rangle(t_c)$, is a key quantity in pulsar population studies. It is found by integrating $f_b(t_c)$ over the distribution functions $P(\alpha_0)$ and $P(\log \tau)$. Using the parameter values from the best fit to the ATNF Cat W_{10} data set, $\langle f_b \rangle(t_c)$ is plotted in Fig. 9 for the three initial alignment models.

Fig. 9 shows strong differences in the $\langle f_b \rangle(t_c)$ among the three models for young pulsars because of the differing initial conditions, with gradual reduction to similar values for older pulsars. The figure implies that the smallness of the observed sample size for old pulsars is significantly influenced by a low probability of observation. Because of completeness issues, and luminosity evolution uncertainty, we cannot evaluate the relative significance of beaming fraction evolution and pulsar ‘death’ (through reducing radio emission) in determining the number of observable old pulsars.

For individual pulsars, the beaming fraction evolution will depend on the pulsar’s α_0 and τ_γ values, but the scaled beaming fraction $f_b(t_c)/\sin \alpha_0$ is independent of α_0 . It is plotted in Fig. 9 for the Model II fit to the ATNF Cat W_{10} data, using various values of τ_γ . It is note-worthy that the scaled beaming fraction is considerably larger for pulsars with a longer alignment time-scale, and so these pulsars are more likely to be observed than those with a small alignment time-scale, even at young ages.

5.4 Alignment time-scales

From Table 3, the best-fitting mean log alignment time-scale, $\mu_{\gamma, \log}$, for Model II is found to be 6.1 ± 0.2 for the ATNF Cat W_{10} fit, 6.1 ± 0.4 for the Parkes MB W_{10} fit, and 5.3 ± 0.4 for the Parkes MB W_{50} fit. The first and last of these three fits have the largest numbers of degrees of freedom, and they agree within two standard deviations of error. Furthermore, a spread in alignment time-scales is needed to accurately model the data (CB86), and for the three fits just mentioned, the standard deviations, σ_{\log} , are 0.83 ± 0.08 , 0.71 ± 0.14 and 1.08 ± 0.09 respectively, indicative of quite a large spread in alignment time-scales about the means.

The *mean* time-scales quoted above are smaller than previous values obtained. The analyses of CB83, CB86 and C93 yielded a

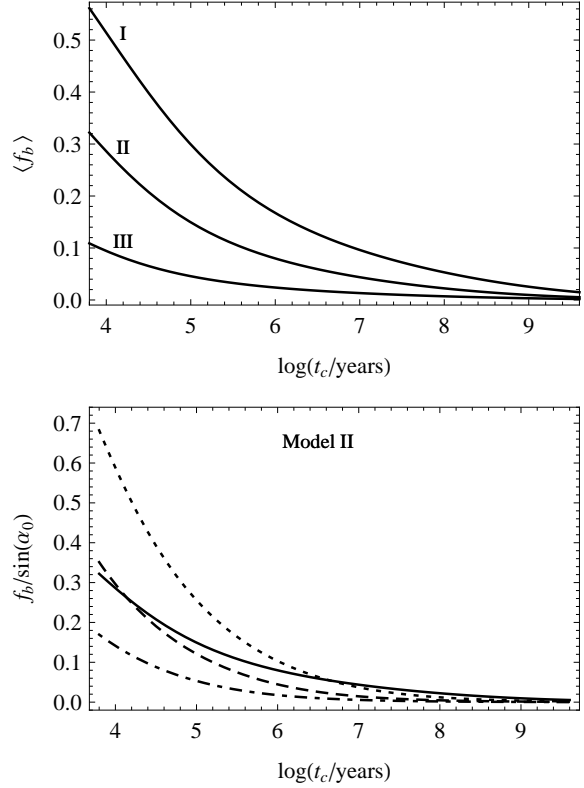


Figure 9. (top) The mean beaming fraction, $\langle f_b \rangle$, is plotted against log characteristic age for Models I, II and III, as labeled. (bottom) The scaled beaming fraction, $f_b/\sin \alpha_0$, is plotted against log characteristic age for Model II. The dashed curve has $\tau_\gamma = \mu_{\gamma, \log}$, the dot-dashed curve has $\tau_\gamma = \mu_{\gamma, \log} - \sigma_{\log}$, and the dotted curve has $\tau_\gamma = \mu_{\gamma, \log} + \sigma_{\log}$. For comparison, the corresponding Model II mean beaming fraction from the top plot is shown as a solid line. Both plots use the the ATNF Cat W_{10} best-fitting parameters, Table 3.

Table 4. Alignment time-scales from different authors.

Authors	Alignment time-scale (yr)
CB83, CB86, C93	2×10^7
Lyne & Manchester (1988)	10^7
Xu & Wu (1991)	1.5×10^7
Kuz'min & Wu (1992)	2×10^7
Tauris & Manchester (1998)	10^7
Weltevrede & Johnston (2008)	7×10^7

mean alignment time-scale of 2×10^7 yr. Other authors have argued in favour of magnetic alignment using different methods and obtained similar alignment time-scales of around 10^7 yr. See for examples Table 4: Lyne & Manchester (1988), Xu & Wu (1991), Kuz'min & Wu (1992) and Tauris & Manchester (1998) all used polarization data, while Weltevrede & Johnston (2008) used interpulse pulsar statistics.

From equation (35), the fitted value of μ_{\log} is determined by the fitted value of $\mu_{\gamma, \log}$ and the value of γ :

$$\mu_{\log} = \mu_{\gamma, \log} - \log(2\gamma), \quad (47)$$

as plotted in Fig. 10. We see that a mean alignment time-scale

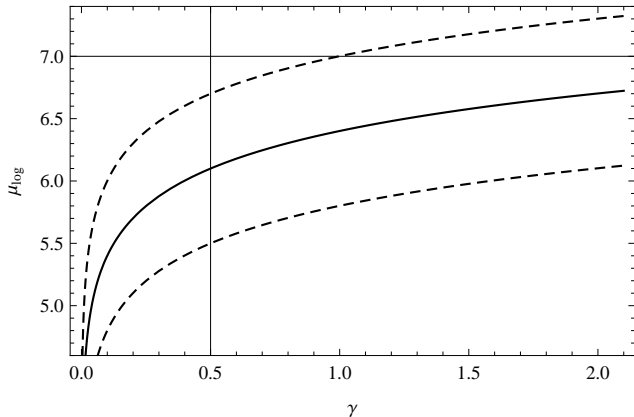


Figure 10. Plots of equation (47): the mean log alignment time-scale, μ_{\log} , as a function of the parameter γ , which was introduced in equation (4). The solid curve corresponds to $\mu_{\gamma,\log} = 6.1$ from the ATNF Cat W_{10} Model II fit (Table 3), and the dashed curves are three standard deviations of error away from the black curve, $\mu_{\gamma,\log} = 6.1 \pm 0.6$. Previous studies have found a log alignment time-scale $\gtrsim 7$. This is inconsistent here with the empirical finding that $\gamma \approx 1/2$.

$10^{\mu_{\log}} \gtrsim 10^7$ yr requires $\gamma > 1$; that is inconsistent with previous findings that γ is between $1/2$ and $2/3$. Conversely, for that range of γ -values, the curves in Fig. 10 give a mean alignment time-scale of around 10^6 yr.

5.5 Pulsar aging

Caution is required in using the characteristic age as a measure of the true ages of pulsars, as will now be explored. Defining $t_\gamma \equiv 2\gamma t$ and using equations (22) and (24) involving τ_γ , it follows from equation (12) for $t(t_c)$ that

$$t_\gamma(t_c) = \frac{\tau_\gamma}{2} \ln \left[1 + \frac{4t_c}{(n_\gamma - 1)\tau_\gamma} \right]. \quad (48)$$

The mean log age, $\langle \log t_\gamma \rangle$, as a function of the log characteristic age, $\log t_c$, is found by integrating over the distribution functions $P(\alpha_0)$ and $P(\log \tau)$. Consider the best fit to the ATNF Cat W_{10} data having parameters as listed in Table 3. A plot of $\langle \log t_\gamma \rangle(\log t_c)$ for Model II is shown in Fig. 11; it shows that that $\langle \log t_\gamma \rangle$ and $\log t_c$ agree up to $\log t_c \sim 10\mu_{\gamma,\log}$, after which time $\langle \log t_\gamma \rangle$ starts to fall below $\log t_c$. The curves for Models I and III are similar.

However, the mean value $\langle \log t \rangle(\log t_c)$ applies to the population as a whole. For individual pulsars, the plots of $\log t(\log t_c)$ depend on the value of τ_γ for that pulsar. Various tracks for individual pulsars are shown in Fig. 11: it is evident that in general the characteristic age diverges much more rapidly from the true age than for the populations mean ages, with the divergence being more rapid the smaller the alignment time-scale. Recall, however, that pulsars with shorter alignment time-scales have a smaller beaming fraction than those with longer time-scales, and so are less likely to be observed.

This highlights the uncertainty that may be present in previous studies that have used the characteristic age as a measure of true age when attempting to measure the alignment time-scales. The characteristic age can over-estimate the true age, and so will tend to give larger alignment time-scales if it is the time measure.

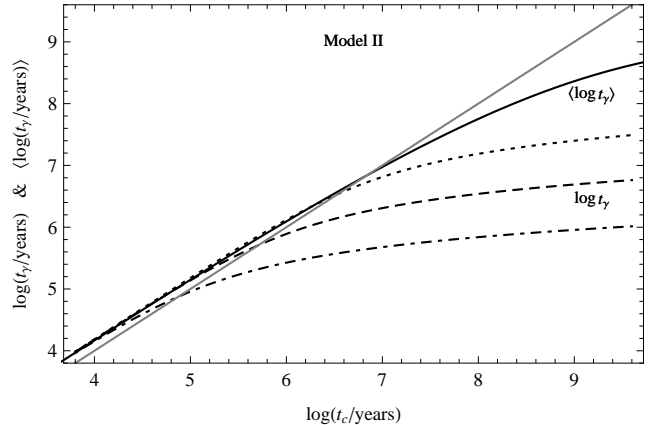


Figure 11. Plots of mean log age, $\langle \log t_\gamma \rangle$, (solid curve) and log age, $\log t_\gamma$, (broken curves) as functions of log characteristic age for Model II: (dashed) $\tau_\gamma = \mu_{\gamma,\log}$, (dot-dashed) $\tau_\gamma = \mu_{\gamma,\log} - \sigma_{\log}$; and (dotted) $\tau_\gamma = \mu_{\gamma,\log} + \sigma_{\log}$. The parameters are from the best fit to the ATNF Cat W_{10} data set (Table 3), and the straight line is $\log t_\gamma = \log t_c$.

6 CONCLUSIONS

From Fig. 6, showing mean pulsewidths versus $\log t_c$, we have seen that the pulsewidth data clearly favour pulsar evolution through magnetic alignment, and not magnetic field decay alone nor progressive counter-alignment. There is a clear minimum of mean pulsewidth at about $t_c \approx 10^{6.9}$ yr. The alignment process causes a significant increase in the mean W_{10} pulsewidth for all characteristic age bins greater than 3×10^7 yr. This is particularly significant in view of the fact that the ATNF catalogue contains numerous pulsars with $t_c > 10^8$ yr, which were not available to the earlier studies.

The three models of initial alignment that were specified in Section 3.3 cannot be tested by fitting the Candy-Blair models to the pulsewidth data alone. However, once a Candy-Blair model has been fitted to the pulsewidth data, it can be used to *predict* mean inclination angle evolution, $\langle \alpha \rangle(\log t_c)$. Comparing these predictions to the datasets of Rankin (1993b) and Gould (1994), it was found that only Model II (a random initial inclination angle) gives a good fit to the data, as shown in Fig. 8.

The alignment time-scale found from fitting Model II to the ATNF Cat W_{10} data (see Tables 1 and 3) is $10^{6.1}$ yr, which is at least a factor of ten shorter than the timescales determined by a number of other authors (see Table 4). The fit requires that the log alignment time-scale varies with a standard deviation of about 0.83 across the observed population. The fit gives a limiting cone opening half-angle of $4^\circ.11$, and a braking index parameter n_γ of 2.30, consistent with the mean, 2.42 ± 0.05 , of the measured apparent braking indices (equations (2) and (25), and Table 2). Consistent with empirical observations, the fit assumes the parameter $\gamma = 1/2$ (see equation (4)). For other values of γ the fitted parameters n and μ_{\log} are determined from equations (21) and (35) respectively. A plot of the mean beaming fraction for this fit is given in Fig. 9.

The initial predictions of pulsar alignment due to electromagnetic braking (Davis & Goldstein 1970; Michel & Goldwire 1970) predicted time-scales of around 10^3 – 10^4 yr, which was rather small. The time-scales will be increased if pulsars are born with their magnetic and rotation axes nearly orthogonal. Jones (1976; 1976a; 1976b) found that the inclusion of a decreasing dissipative torque initially brought all pulsars close to counter-alignment, from which time the normal electromagnetic decay of α would begin.

Jones predicted that the alignment phase started at around 10^3 – 10^4 yr, with a time-scale of around 10^6 yr, which was believed to be more in accord with the observed population.

We have found alignment time-scales consistent with the predictions of Jones, though with a significant spread in values, down to the time-scales consistent with the absence of the counter-alignment phase. Contrary to the model of Jones, though, we do not find evidence for all pulsars starting their alignment phase with α_0 close to 90° (i.e. Model I). This interesting counter-point to the model of Jones deserves further investigation.

ACKNOWLEDGMENTS

We thank the Australia Telescope National Facility for making their pulsar database available. We thank R. N. Manchester for many helpful discussions and comments on the manuscript, and the referee of an earlier version of this paper for a helpful review.

REFERENCES

- Beskin V. S., Gurevich A. V., Istomin Y. N., 1984, *Ap&SS*, 102, 301
 Camilo F., Kaspi V. M., Lyne A. G., Manchester R. N., Bell J. F., D’Amico N., McKay N. P. F., Crawford F., 2000, *ApJ*, 541, 367
 Candy B. N., 1993, PhD thesis, University of Western Australia
 Candy B. N., Blair D. G., 1983, *MNRAS*, 205, 281
 Candy B. N., Blair D. G., 1986, *ApJ*, 307, 535
 Davis L., Goldstein M., 1970, *ApJ*, 159, L81
 Gil J. A., Han J. L., 1996, *ApJ*, 458, 265
 Gould D. M., 1994, PhD thesis, The University of Manchester
 Gunn J. E., Ostriker J. P., 1970, *ApJ*, 160, 979
 Johnston S., Galloway D., 1999, *MNRAS*, 306, L50
 Jones P. B., 1976a, *Nature*, 262, 120
 Jones P. B., 1976b, *ApJ*, 209, 602
 Jones P. B., 1976, *Ap&SS*, 45, 369
 Kuz’min A. D., Wu X., 1992, *Ap&SS*, 190, 209
 Livingstone M. A., Kaspi V. M., Gavriil F. P., 2005, *ApJ*, 633, 1095
 Livingstone M. A., Kaspi V. M., Gavriil F. P., Manchester R. N., 2005, *ApJ*, 619, 1046
 Livingstone M. A., Kaspi V. M., Gavriil F. P., Manchester R. N., Gotthelf E. V. G., Kuiper L., 2007, *Ap&SS*, 308, 317
 Livingstone M. A., Kaspi V. M., Gotthelf E. V., Kuiper L., 2006, *ApJ*, 647, 1286
 Lorimer D. R., Faulkner A. J., Lyne A. G., Manchester R. N., Kramer M., McLaughlin M. A., Hobbs G., Possenti A., Stairs I. H., Camilo F., Burgay M., D’Amico N., Corongiu A., Crawford F., 2006, *MNRAS*, 372, 777
 Lyne A. G., Manchester R. N., 1988, *MNRAS*, 234, 477
 Lyne A. G., Pritchard R. S., Graham-Smith F., Camilo F., 1996, *Nature*, 381, 497
 Lyne A. G., Pritchard R. S., Smith F. G., 1993, *MNRAS*, 265, 1003
 Lyne A. G., Smith F. G., 2006, *Pulsar Astronomy*, 3rd ed.. Cambridge University Press, Cambridge
 Manchester R. N., Han J. L., Qiao G. J., 1998, *MNRAS*, 295, 280
 Manchester R. N., Hobbs G. B., Teoh A., Hobbs M., 2005, *AJ*, 129, 1993
 Manchester R. N., Lyne A. G., Camilo F., Bell J. F., Kaspi V. M.,

- D’Amico N., McKay N. P. F., Crawford F., Stairs I. H., Possenti A., Morris D. J., Sheppard D. C., 2001, *MNRAS*, 328, 17
 Manchester R. N., Taylor J. H., 1977, *Pulsars*. Freeman, San Francisco
 Manchester R. N., Taylor J. H., 1981, *AJ*, 86, 1953
 McKinnon M. M., 1993, *ApJ*, 413, 317
 Michel F. C., Goldwire Jr. H. C., 1970, *Astrophys. Lett.*, 5, 21
 Narayan R., Ostriker J. P., 1990, *ApJ*, 352, 222
 Pandey U. S., Prasad S. S., 1996, *A&A*, 308, 507
 Phinney E. S., Blandford R. D., 1981, *MNRAS*, 194, 137
 Press W. H., Teukolsky S. A., Vetterling W. T., Flannery B. P., 1992, *Numerical Recipes: The Art of Scientific Computing*, 2nd edition. Cambridge University Press, Cambridge
 Rankin J. M., 1993a, *ApJ*, 405, 285
 Rankin J. M., 1993b, *ApJS*, 85, 145
 Ruderman M. A., Sutherland P. G., 1975, *ApJ*, 196, 51
 Tauris T. M., Konar S., 2001, *A&A*, 376, 543
 Tauris T. M., Manchester R. N., 1998, *MNRAS*, 298, 625
 Wang N., Manchester R. N., Zhang J., Wu X. J., Yusup A., Lyne A. G., Cheng K. S., Chen M. Z., 2001, *MNRAS*, 328, 855
 Weltevrede P., Johnston S., 2008, *MNRAS*, 387, 1755
 Xilouris K. M., Kramer M., Jessner A., Wielebinski R., Timofeev M., 1996, *A&A*, 309, 481
 Xu W., Wu X., 1991, *ApJ*, 380, 550

APPENDIX A: PULSEWIDTH AVERAGING INTEGRAL

The integral that averages the pulsewidth over a random distribution of viewing angles can be evaluated analytically, as follows. As above, α is the pulsar magnetic-spin inclination angle, ρ the emission cone half-width, and ζ is the angle between the observer’s direction and the pulsar’s spin axis.

A1 Observer dependence of pulsewidth

For an individual pulsar, the variation of its observed angular pulsewidth with observer viewing angle is given by the formula (Manchester & Taylor 1977, p. 218)

$$W(\alpha, \rho, \zeta) = 2 \arccos \left(\frac{\cos \rho - \cos \alpha \cos \zeta}{\sin \alpha \sin \zeta} \right), \quad (\text{A1})$$

which is equation (26) in the main text above.

In considering the variation of W with viewing angle, it is helpful to employ the variable $x \equiv \cos \zeta$. Equation (A1) takes the form

$$W(\alpha, \rho, x) = 2 \arccos[f(x)], \quad (\text{A2})$$

with the abbreviations

$$f(x) \equiv \frac{1}{\sin \alpha} \frac{b - ax}{(1 - x^2)^{1/2}}, \quad a \equiv \cos \alpha, \quad \text{and} \quad b \equiv \cos \rho. \quad (\text{A3})$$

Note that

$$(\sin \alpha) f'(x) = (bx - a)/(1 - x^2)^{3/2} \quad \text{and} \quad (\text{A4})$$

$$(\sin \alpha) f''(x) = (b - 3ax + 2bx^2)/(1 - x^2)^{5/2}. \quad (\text{A5})$$

The function $f(x)$, which is just the cosine of the pulse angular half-width, is < 1 throughout the cut across the emission beam by the sight line to any ‘illuminated’ observer. It reaches 1 in magnitude (i.e. $f^2 = 1$) at the pulse visibility limits $\zeta = |\alpha \mp \rho|$,

corresponding to $x = x_{\pm}$, where

$$x_{\pm} \equiv \cos(\alpha \mp \rho) = ab \pm \Delta \quad \text{with} \quad (\text{A6})$$

$$\Delta \equiv (1 - a^2)^{1/2}(1 - b^2)^{1/2}. \quad (\text{A7})$$

Substituting (A6) into (A3) gives

$$f(x_{\pm}) = \frac{b(1 - a^2)^{1/2} \mp a(1 - b^2)^{1/2}}{[1 - (ab \pm \Delta)^2]^{1/2}}. \quad (\text{A8})$$

This shows that at x_{-} , the ‘outer’ visibility limit, f is always positive, i.e. $+1$. At x_{+} , the ‘inner’ visibility limit, f is $+1$ for $\alpha > \rho$, 0 for $\alpha = \rho$, and -1 for $\rho > \alpha$. Let’s visualize these three cases in turn.

(1) For $\alpha > \rho$, the visibility limits x_{\pm} both correspond to zero pulsewidth, $W(x) = 0$. Equations (A4) and (A5) show that the minimum value $(b^2 - a^2)^{1/2}/(\sin \alpha)$ of $f(x)$ – corresponding to the greatest pulsewidth – occurs for the cone of observers at $x = a/b$:

$$W_{\max} = 2 \arccos \left\{ [1 - (\sin \rho)^2 / (\sin \alpha)^2]^{1/2} \right\} \quad (\text{A9})$$

at $\cos \zeta = (\cos \alpha) / (\cos \rho)$.

(2) For $\alpha = \rho$, one can visualize the emission cone as rolling around the spin axis, which is then the inner visibility limit. In this case, $f(x) = (\cot \alpha)[(1 - x)/(1 + x)]^{1/2}$; also $x_{+} = +1$ (observer looking along the spin axis) so $f(x_{+}) = 0$, corresponding to $W(x_{+}) = \pi$. So $W(x)$ increases monotonically from 0 at the outer visibility limit to π on the spin axis in this special case.

(3) For $\rho > \alpha$, the beam will be ‘always on’ (unpulsed) to observers within $(\rho - \alpha)$ of the spin axis. So the pulse visibility limit x_{+} then corresponds to $W = 2\pi$, with $f(x)$ ranging from $+1$ at x_{-} to -1 at x_{+} , with no minimum: $W(x)$ increases monotonically from 0 at the outer visibility limit to 2π at the inner one.

A2 Evaluating the averaging integral

Integrating equation (A1) for $W(\alpha, \rho, \zeta)$ over a random distribution of viewing angles, using the observer distribution function $(\sin \zeta)/(2f_b)$, gives the mean angular pulsewidth, for pulsars of given α and ρ :

$$\langle W \rangle(\alpha, \rho) = (2f_b)^{-1} \int_{|\alpha - \rho|}^{\alpha + \rho} W(\rho, \alpha, \zeta) \sin \zeta \, d\zeta \quad (\text{A10})$$

$$= f_b^{-1} \int_{x_{-}}^{x_{+}} \arccos[f(x)] \, dx. \quad (\text{A11})$$

It is integration of the observer distribution function $(\sin \zeta)/2$ over the same range that yields the beaming factor $f_b = \sin \alpha \sin \rho$.

Note for use below that

$$(\sin \alpha) [1 - f^2(x)]^{1/2} = G^{1/2}(x)/(1 - x^2)^{1/2}, \quad (\text{A12})$$

$$\text{with } G(x) \equiv (x - x_{-})(x_{+} - x). \quad (\text{A13})$$

The function $G(x)$ describes an inverted parabola: it is zero at the limits of integration x_{\pm} and positive in between, with a maximum value $(1 - a^2)(1 - b^2) = \sin^2 \alpha \sin^2 \rho (= f_b^2)$ at $x = ab = \cos \alpha \cos \rho$.

Applying integration by parts in equation (A11) for $\langle W \rangle$ reduces the problem to one of evaluating an integral of an algebraic function. Using $d(\arccos X) = -(1 - X^2)^{-1/2} dX$ together with equations (A4) and (A12) for df/dx and $(1 - f^2)^{1/2}$ gives

$$\langle W \rangle(\alpha, \rho) f_b = x_{+} \arccos[f(x_{+})]$$

$$+ \int_{x_{-}}^{x_{+}} \frac{x(bx - a) \, dx}{(1 - x^2)G^{1/2}(x)}, \quad (\text{A14})$$

because the integrated part $x \arccos[f(x)]$ – which by equation (A2) is just $x W(x)/2$ – always vanishes at the limit x_{-} , where $f = +1$ always. The first term on the RHS of equation (A14) is

$$\begin{aligned} & 0 \quad \text{for } \alpha > \rho \quad [f(x_{+}) = +1], \\ & \pi/2 \quad \text{for } \alpha = \rho \quad [f(x_{+}) = 0, x_{+} = +1], \\ & \pi \cos(\rho - \alpha) \quad \text{for } \alpha < \rho \quad [f(x_{+}) = -1]. \end{aligned} \quad (\text{A15})$$

Re-arranging the integrand in equation (A14) gives

$$\begin{aligned} \langle W \rangle(\alpha, \rho) f_b &= \frac{x_{+}}{2} W(x_{+}) \\ &+ \int_{x_{-}}^{x_{+}} \left(\frac{b - a}{2(1 - x)} + \frac{b + a}{2(1 + x)} - b \right) \frac{dx}{G^{1/2}(x)}. \end{aligned} \quad (\text{A16})$$

This result shows that we can employ the following indefinite integrals, in which Δ and G are defined by equations (A7) and (A13):

$$\int G^{-1/2}(x) \, dx = \arcsin[(x - ab)/\Delta] \quad \text{and} \quad (\text{A17})$$

$$\begin{aligned} \int \frac{dx}{(1 \pm x)G^{1/2}(x)} &= \int \frac{dx}{(1 \pm x)[(x - x_{-})(x_{+} - x)]^{1/2}} \\ &= \frac{2}{|a \pm b|} \arctan \sqrt{\frac{(x - x_{-})(1 \pm x_{+})}{(x_{+} - x)(1 \pm x_{-})}}, \end{aligned} \quad (\text{A18})$$

where $x_{\pm} = ab \pm \Delta$ and equation (A7) for Δ have been used.

So the required definite integrals are

$$\int_{x_{-}}^{x_{+}} G^{-1/2}(x) \, dx = \pi, \quad \text{and} \quad (\text{A19})$$

$$\int_{x_{-}}^{x_{+}} \frac{dx}{(1 \pm x)G^{1/2}(x)} = \frac{\pi}{|a \pm b|}. \quad (\text{A20})$$

Thanks to these definite integrals, equation (A16) for the observer-averaged pulsewidth evaluates to

$$\langle W \rangle(\alpha, \rho) f_b = \frac{x_{+}}{2} W(x_{+}) + \frac{\pi}{2} [\text{sign}(b - a) + 1 - 2b]. \quad (\text{A21})$$

That is:

$$\langle W \rangle(\alpha, \rho) f_b = \begin{cases} [1 - \cos \rho] \pi & \text{for } \alpha \geq \rho, \\ [\cos(\rho - \alpha) - \cos \rho] \pi & \text{for } \alpha \leq \rho, \end{cases} \quad (\text{A22})$$

as used in the main text – equation (38) above.